

Template for preparing your research report submission to PNAS using Overleaf

Author One^{a,c,1}, Author Two^{b,1,2}, and Author Three^a

^aAffiliation One; ^bAffiliation Two; ^cAffiliation Three

This manuscript was compiled on August 16, 2017

We present a conceptual and computational framework to unify today's theories of neuromuscular control called feasibility theory. We begin by describing how the musculoskeletal anatomy of the limb, the need to control individual tendons, and the physics of a motor task uniquely specify the family of all valid muscle activations that accomplish it (its 'feasible activation space'). For our example of static force production with a finger with seven muscles, computational geometry characterizes, in a complete way, the structure of feasible activation spaces as 3-dimensional polytopes embedded in 7-D. The feasible activation space for a given task is the landscape where all neuromuscular learning, control, and performance must occur. This approach unifies current theories of neuromuscular control because the structure of feasible activation spaces can be separately approximated as either low-dimensional basis functions (synergies), high-dimensional joint probability distributions (Bayesian priors), or fitness landscapes (to optimize cost functions).

Neuromechanics | Motor Control | Tendon actuation | ...

This PNAS journal template is provided to help you write your work in the correct journal format. Instructions for use are provided below.

Note: Please start your introduction without including the word "Introduction" as a section heading (except for math articles in the Physical Sciences section); this heading is implied in the first paragraphs.

Introduction

How the nervous system selects specific levels of muscle activations (i.e. a muscle activation pattern) for a given motor task continues to be hotly debated. Some suggest the nervous system either combines low-dimensional synergies (? ? ? ? ?), learns probabilistic representations of valid muscle activation patterns (? ? ? ?), or optimizes physiologically-tenable cost functions (? ? ? ? ? ?). At the core of this problem lies the nature of 'feasible activation spaces,' and the computational challenge of describing and understanding their high-dimensional structure (for an overview, see (?)). A feasible activation space is the family of valid solutions (i.e. muscle activation patterns) available to the nervous system to produce a given motor task. Fig. 1 illustrates the neuromechanical interactions that define the feasible activation space for a particular task.

The most the nervous system can do, therefore, is select a specific muscle activation pattern from within the feasible activation space—as muscle activation patterns outside of this space are, by definition, inappropriate for the task. In fact, the feasible activation space defines the landscape upon which all neuromuscular learning and performance must occur. Understanding neuromuscular control is, therefore, equivalent to understanding how the nervous system finds, explores, inhab-

its, and exploits the structure of feasible activation spaces (? ? ? ? ? ? ?).

But the 'curse of dimensionality' (? ? ?) makes it computationally challenging to calculate, describe, and understand the nature and structure of high-dimensional feasible activation spaces (? ? ? ? ? ? ?)—even for an isolated human finger or cat leg generating everyday static forces (? ? ? ?). This is due to the computational complexity of algorithms applied upon high dimensional spaces.

Current theories of neuromuscular control are alternative responses to the curse of dimensionality, which at times can be seen as competing, rather than complementary. However, the fundamental neuromechanics of the limb and the physics of the task are the common ground for all theories. Thus, understanding the nature and structure of feasible activation spaces would help compare, contrast and combine these alternative approaches to neuromuscular control.

We now propose a conceptual and computational framework to provide complete characterizations of feasible activation spaces, thereby contextualizing and unifying multiple theories of neuromuscular control. As an example, we leverage prior work (? ? ?) to now describe the structure of the feasible activation space for the seven muscles of the index finger when producing static fingertip force. This is the type of fingertip force observed when, for example, pressing hard on a table without finger movement, and is also referred to as an isometric force task. In this case, the feasible activation space is a polytope embedded in 7-dimensional muscle activation space. A polytope is the name given to bounded convex polyhedra in dimensions higher than 3. Our computational approach hinges on the efficient sampling and complete representation of the structure of high-dimensional polytopes. This then character-

Significance Statement

Wings take flight, eyes refract light, and muscles manipulate bones within the interplaying constraints of Newtonian physics. Here we apply the basic tenets of physics to the field of neuromechanical control, to elucidate the neuro-physical-motor landscape upon which evolution and learning operate. With three interweaving hypotheses of motor control in the literature, we fill the gap between the disparate approaches by recontextualizing the problem of force control as a physical constraints problem, thereby lighting the stage of optimal, synergistic, and bayesian control.

Please provide details of author contributions here.

Please declare any conflict of interest here.

¹A.O.(Author One) and A.T. (Author Two) contributed equally to this work (remove if not applicable).

²To whom correspondence should be addressed. E-mail: author.two@email.com

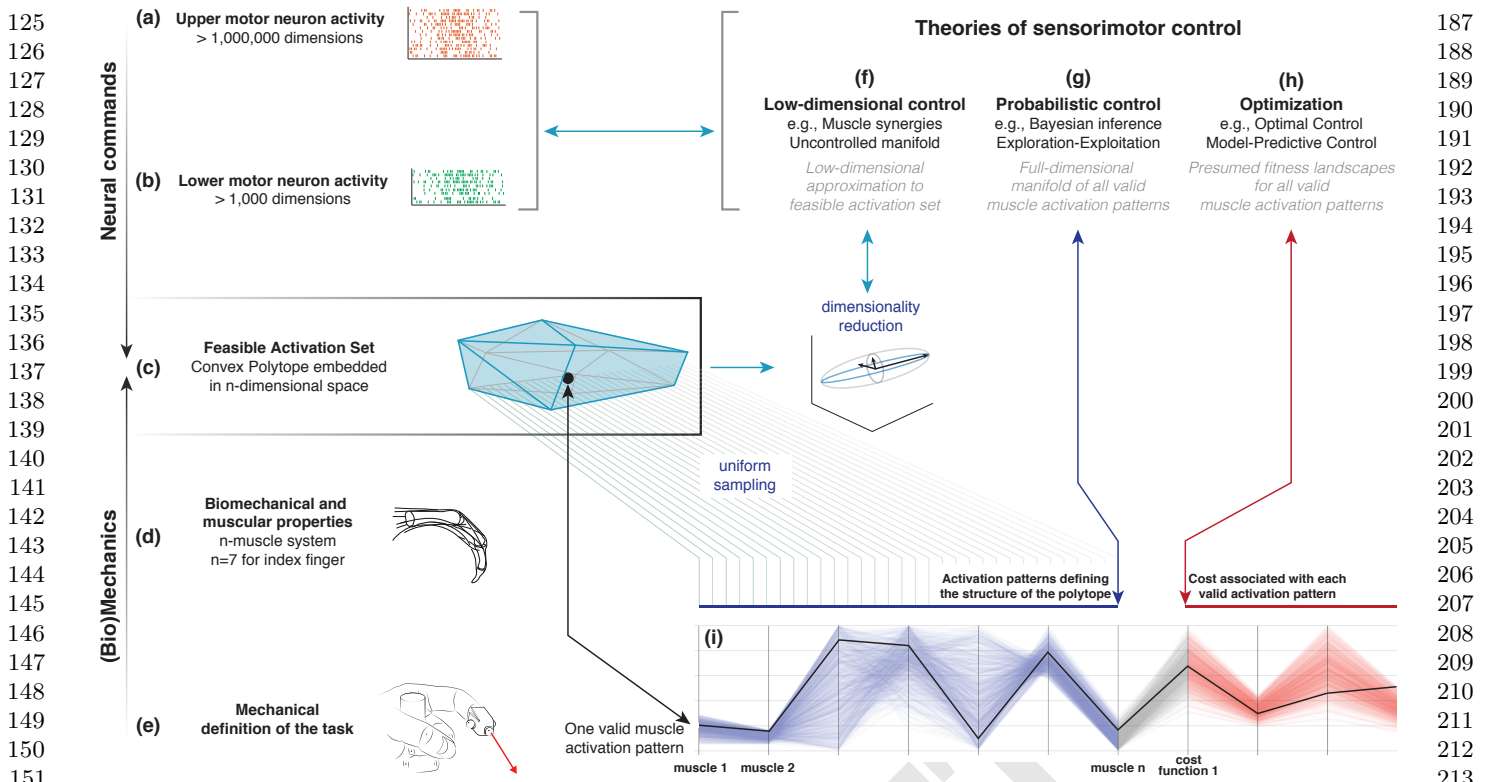


Fig. 1. Feasible activation spaces guiding sensorimotor control of a task. The descending motor command for a given task is issued by the primary motor cortex (a), which projects onto alpha-motor neuron pools in the spinal cord (b). The combined drive to all alpha-motor neurons of a muscle can be considered its total muscle activation level (a value between 0 and 1). If we consider that motor commands are sent to multiple independently controlled muscles, then the overall motor command can be conceptualized as a multi-dimensional muscle activation pattern (i.e., a point) in a high-dimensional muscle activation space (?? ? ? ?) (c). For that muscle activation pattern to be valid, it has to elicit muscle forces (d) capable of satisfying the mechanical requirements of the task—in this case a well directed fingertip force (e). Given the large number of muscles in vertebrates, there is muscle redundancy; there is a large number of valid muscle activation patterns that can produce a given task. We propose that our novel ability to characterize the high-dimensional structure of feasible activation spaces (i) allows us to compare, contrast and reconcile today's three dominant approaches to redundancy in sensorimotor control (f, g, h).

152
153
154
155
156
157
158
159
160
161
162
163
164
165
166
167
168
169
170
171
172
173
174
175
176
177
178
179
180
181
182
183
184
185
186
izes all valid muscle activation patterns. These computational techniques can scale up to ~40 dimensions, which suffices to analyze the neural control of all muscles in an extant vertebrate limb systems. By providing a complete characterization of all muscle activation patterns for a given motor task, we are able to compare, contrast, combine—and reconcile—today's three dominant approaches to neuromuscular control.

Results

The goal of this work is to use different perspectives to describe the high-dimensional structure of these feasible activation spaces; we then show how these spaces allow us to unify today's theories of neuromuscular control. We used our realistic index finger model to calculate the feasible activation space for the task of producing static fingertip force in the distal direction (see Fig. 1). The model represents each muscle's contribution to fingertip force as a directed force vector at the fingertip; there are 7 of these force vectors at the index fingertip. As described briefly in the Methods, Hit-and-Run is a method in polytope sampling that we use to sample from the infinite number of muscle activations within the feasible activation space. In effect, given a fingertip task force and the maximum linear fingertip forces each muscle creates, we can collect the muscle activations required to produce that task. As we can now collect thousands of muscle activation patterns for any

isometric force task, we examined how the feasible activation spaces (and their representations) change with increasing task intensity in the distal direction (Fig. 1e).

We collected points for multiple task intensities between 0% (i.e., pure co-contraction without output force) and 100% of maximal static force.

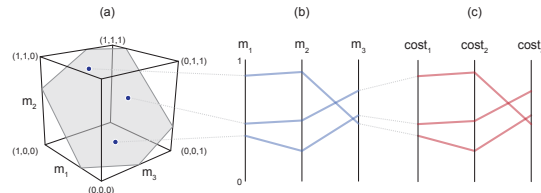


Fig. 2. Characterizing the high-dimensional structure of a feasible activation space via parallel coordinates. Consider three points (i.e., muscle activation patterns in Supplemental Fig. ??e) from the feasible activation space (a). The activation level for each muscle (i.e., the coordinates of each point) are sewn across three vertical parallel axes (b). As is common when evaluating multiple valid coordination patterns, each point can be assigned a cost as per an assumed cost function. The associated cost for each muscle activation pattern can also be shown as an additional dimension. We show three representative cost functions (c). Activation levels are bound between 0 and 1, and costs are normalized to their respective observed ranges.

249
250
251
252
253
254
255
256
257
258
259
260
261
262
263
264
265
266
267
268
269
270
271
272
273
274
275
276
277
278
279
280
281
282
283
284
285
286
287
288
289
290
291
292
293
294
295
296
297
298
299
300
301
302
303
304
305
306
307
308
309
310

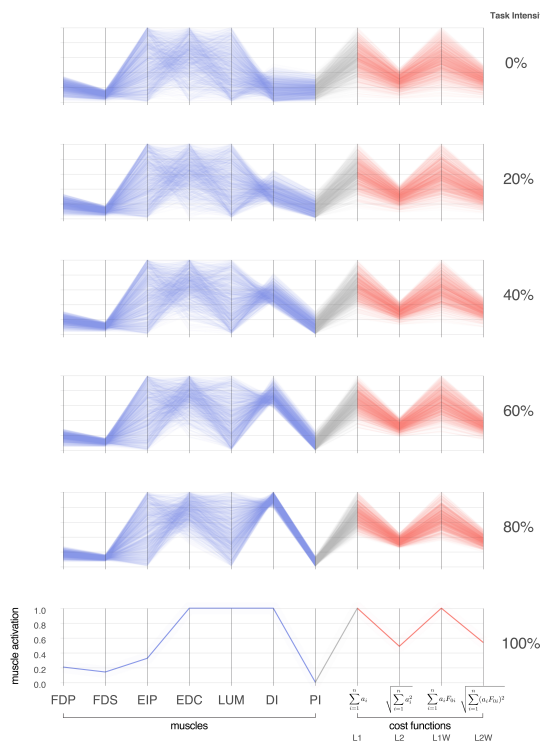


Fig. 3. Activation patterns of the seven muscles of the index finger across six magnitudes of a fingertip force The connectivity across parallel coordinates shows how muscle activation patterns are related in multiple ways to produce a fingertip force vector between 0 (a) to 100% (f) of maximal magnitude. At these extremes we have, respectively, the coordination patterns that produce pure co-contraction and the one unique solution for maximal output. In between, we see the how the structure of the feasible activation spaces changes as redundancy is lost. In blue are the activation values, and in red are normalized costs for four cost functions common in the literature. *FDP*: flexor digitorum profundus, *FDS*: flexor digitorum superficialis, *EIP*: extensor indicis proprius, *EDC*: extensor digitorum communis, *LUM*: lumbrical, *DI*: dorsal interosseous, *PI*: palmar interosseous.

Parallel coordinate visualization naturally reveals the structure of the feasible activation space. We used Hit-and-Run to sample from feasible activation spaces for 6 task intensities, labeled as task intensities α of 0.0, 0.2, 0.4, 0.6, 0.8 and 1.0. For each task intensity, we ran 100,000 Hit-and-Run iterations and down-sampled to every 100th point to produce 1,000 points that are (in our experiments) uncorrelated and uniformly distributed in P . Recall that approaching 100% of maximal force shrinks P to a single, unique solution (?).

Parallel coordinate visualization effectively reveals correlations that exist among the 1,000 valid muscle activation patterns for each magnitude of desired fingertip force, and activation pattern cost, Fig. 2 and Fig. 3.

An interactive parallel coordinate visualization plot can be accessed at <https://briancohn.github.io/space-parcoords/>. This interactive interface for parallel coordinate visualization allows us to explore subsets of the valid muscle activation patterns.

For example, restricting the range of muscle activation of one or more muscles shows us the necessary activation levels of the remaining muscles. This can be used to, say, simulate a 40% reduction in possible activation to some muscles (e.g., due to a peripheral neuropathy) in the extrinsic extensor muscles of the index finger innervated by the radial nerve (EIP and EDC) (?).

Figures in the Supplemental Material show how, for 80% of task intensity (i.e., 80% of maximal force output), only 29% (i.e., $\frac{290}{1,000}$) of all possible solutions survive when capping the maximal excitation of EIP and EDC at 60%. Thus, any neural or muscle dysfunction that compromises the ability of the extensor muscles will limit the choices the nervous system has to produce this force—even at sub-maximal levels. These results further challenge the notion of muscle redundancy as discussed in detail in (? ?).

Moreover, this same case of task intensity of 80% and maximal excitation of EIP $\leq 60\%$ reveals important and counterintuitive consequences in the control of musculature. For example, the range of feasible activation level for some muscles do not change too much (FDP, FDS, and LUM), but does change for others (DI and PI). Most interestingly, the range of costs across valid solutions remains broad.

Similarly, we can describe any subset of muscle activation patterns associated with specific ranges for a given cost function. Figures in the Supplemental Material also show how can characterize all muscle activation patterns associated with the lowest 10% of L2 weighted costs. The coordination patterns that meet this strict criterion are quite different from one another (note the broad ranges and criss-cross patterns).

These relationships among all valid 7-dimensional muscle activations patterns reveal important aspects of the structure of the feasible activation space, and its associated cost landscapes. We see one muscle can affect other muscles in different ways: while limiting PI to 20% of maximal activation eliminates 30.1% of the valid solutions, limiting DI to 20% eliminates 42.8% of them. Similarly we can distinguish between changes in the extreme values of muscle activation from changes in the number of valid solutions. Consider the range of activation for DI and PI at task intensity of 80% which lies between 0 and 0.52 and 0.39, respectively. Limiting DI to 20% pulls PI's maximum down by nearly 0.20, and the converse

311
312
313
314
315
316
317
318
319
320
321
322
323
324
325
326
327
328
329
330
331
332
333
334
335
336
337
338
339
340
341
342
343
344
345
346
347
348
349
350
351
352
353
354
355
356
357
358
359
360
361
362
363
364
365
366
367
368
369
370
371
372

373 has nearly the same effect. However, in both cases, the median
 374 activation among surviving solutions changes no more than
 375 0.06. This emphasizes that understanding feasible activation
 376 spaces requires and understanding of its internal density and
 377 not just its bounds. The density of **between-muscle** connec-
 378 tivity is seen directly by the density of the lines connecting
 379 the different muscles and cost functions. The **within-muscle**
 380 density can be computed by binning points at each activation
 381 level value.

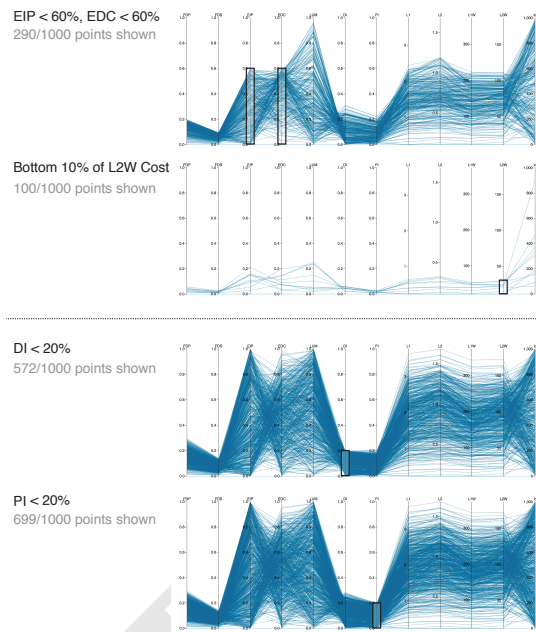
382 Lastly, those same connecting lines in the parallel coordi-
 383 nate visualization allow us to characterize the interrelatedness
 384 of valid solutions in 7-dimensional space. For example, the
 385 lines connecting FDP and FDS are mostly parallel, indicating
 386 a strong positive correlation. In fact, looking at these lines
 387 allows one to directly see and understand the Pearson product-
 388 moment correlation coefficients of 0.99, -0.50, and -0.06 in the
 389 adjacent muscle pairs FDP—FDS, LUM—DI, and EIP—EDC,
 390 respectively. The interactive parallel coordinate visualization
 391 also allows for any pairwise comparison by simply dragging
 392 and reordering the vertical axes—and hovering over individual
 393 data rows highlight an individual valid activation pattern atop
 394 all others.

395 **Low-dimensional approximations to the feasible activation
 396 space.** We applied PCA (Principal Component Analysis) to
 397 the valid muscle activation patterns sampled uniformly at
 398 random from the feasible activation space. We show results for
 399 10 levels of task intensity. However, we did this in an iterative
 400 fashion to replicate the fact that experimental studies can only
 401 collect a finite amount of data from each subjects. Thus, from
 402 the total pool of 10,000 sub-sampled points sampled by Hit-
 403 and-Run (i.e., accepting every 100th point from 100,000 total
 404 samples to remove potential autocorrelation among points);
 405 sample sizes of 10, 100, and 1,000 points (i.e., simulated ‘ex-
 406 perimental’ sample sizes) were replicated 100 times each. We
 407 applied PCA to each set of sampled points.

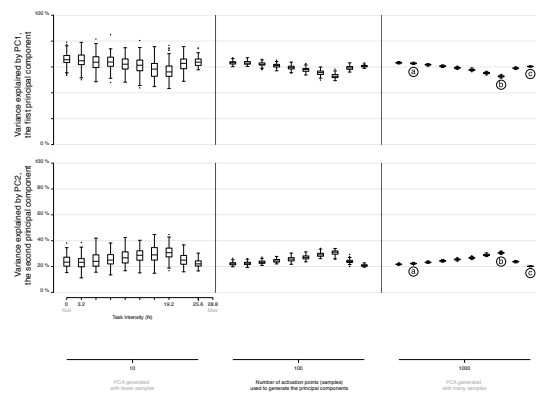
408 The variance explained by PC1 and PC2 (and its boxplot
 409 distribution) for all iterations are shown to change with task
 410 intensity for all sample sizes (Fig. 5). Explaining about 13–15%
 411 of the variance, PC3 is exactly equal to the remaining variance
 412 not explained by the first two components—this is a result of
 413 the feasible activation space being a 3-dimensional polytope
 414 P by construction (i.e., recall that 4 task constraints applied
 415 to 7 muscles produce a 3-dimensional polytope embedded in
 416 the 7-dimensional muscle activation space).

417 The boxplots in Fig. 5 quantify how different amounts of
 418 data change the estimates of variance explained by PC1 and
 419 PC2 with task intensity (c.f. labels a vs. b vs. c). We see
 420 this dispersion is small in the center and right columns. Note
 421 that the ratio of variance explained between PC1 and PC2
 422 between 50 to 80% of task intensity is indicative of changes in
 423 the aspect ratio of the feasible activation space—which we see
 424 changes with task intensity.

425 Importantly, using experimentally realistic samples sizes of
 426 10 repetitions per subject (leftmost column) not only does not
 427 capture this change, but its standard deviation is large enough
 428 to blur the statistically significant differences that are known
 429 to appear with larger (but experimentally unrealistic) sample
 430 sizes. The impact of impoverishing the number of samples fed
 431 to PCA reminds us that inadequate amounts of data obfuscate
 432 the underlying changes in the structure of the data analyzed
 433 (Fig. 5).



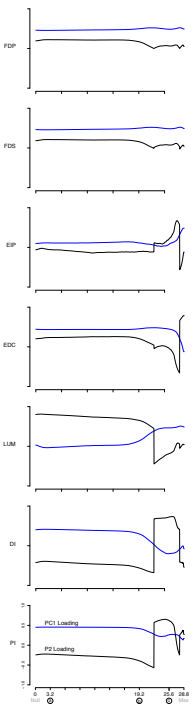
499 **Fig. 4. Supplemental Figure: Posthoc constraints on a task intensity of 80%**
 500 Here we show four unique examples of constraints applied to the points collected
 501 from the feasible activation space. With this, we can rapidly predict how index finger
 502 control must change in the event of weakness in specific muscles. We also can see
 503 how many points remain once the constraints are added—signaling how the structure
 504 of the feasible force space is affected.



505 **Fig. 5. Approximating the structure of feasible activation spaces via principal
 506 components analysis (PCA) is sensitive to both the number of points used and
 507 the intensity of the task.** Rows show the variance explained by the first (top) and
 508 second (bottom) principal components with increasing data points (left to right). It is
 509 not possible to generalize the variance explained across tasks intensities, and large
 510 numbers of points (i.e., > 100) are needed to confidently estimate the real changes
 511 in variance explained as a function of task intensity (cf. points labeled a, b, c).

497 There were also important changes in the loadings of the
 498 PC1 and PC2 vectors. While the ratio of variance explained
 499 between PC1 and PC2 gives a sense of the aspect ratio of
 500 the feasible activation space, the loadings of PC1 and PC2
 501 speak to its orientation. Fig. 6 shows how the loadings of
 502 the PC1 and PC2 vectors change across labels a, b, and c
 503 (Fig. 5) corresponding to 11, 66 and 88% of task intensity,
 504 respectively. What these loadings indicate are the direction in
 505 7-dimensional space, which changes dramatically.

506 These changes we see in (i) the lower and upper bounds of
 507 activations, and in (ii) the relative variance explained and (iii)
 508 loadings for PC1 and PC2, demonstrate that the size, shape
 509 and orientation of the feasible activation space changes with
 510 task intensity. Moreover, these changes represent the best-case
 511 scenario given the absence of experimental noise, within- and
 512 across-subject variability, and measurement error.



540 **Fig. 6. PCA loadings change dramatically as task intensity increases** For each
 541 of 1,000 task intensities, we collected 1,000 points from the feasible activation space,
 542 and computed three principal components. Note that the signs of the loadings depend
 543 on the numerics of the PCA algorithm, and are subject to arbitrary flips in sign—
 544 thus for clarity we plot them such that FDP's loadings in PC1 are positive at all
 545 task intensities. Synergies at representative task intensities a, b, c in Fig. 5 differ.
 546 This reflects changes in the geometric structure of the feasible activation space as
 547 redundancy is lost.

548 **Changes in the probabilistic structure of the feasible activation space with increasing task intensity, or how muscle redundancy is lost.** The maximal static fingertip force vector in
 549 a given direction is produced by a single and unique combination of muscle activations. In contrast, any sub-maximal
 550 magnitude of that same vector is produced by an infinite number of solutions (? ? ? ?). Our analysis of feasible activation
 551 spaces at different task intensities allows us to characterize how
 552 this redundancy changes and is lost. The histogram heatmaps
 553 in Fig. 7 illustrate the changes and shrinking of within-muscle
 554

555 density of valid activation levels for sub-maximal forces, converging to a single solution for maximal force output. These
 556 surface plots show how the normalized histograms (of 1,000
 557 valid activation levels for each muscle) change at each of 100
 558 levels of task intensity between 0 and 1. Following a muscle's
 559 column from bottom to top shows the activation histograms
 560 for each magnitude of distal force and ending, naturally, with
 561 a spike about the unique value at maximal force production.

562 The flat areas in each surface plot (e.g. clearly visible
 563 for DI) represent muscle activation levels that are not valid
 564 for that task intensity. That is, there exist no valid muscle
 565 activation patterns that contain that muscle at that level, and
 566 thus no points are found there.

567 These plots show the nature and rate of convergence to the
 568 unique solution for maximal force output across muscles. We
 569 find that the histograms of activation levels for each muscle
 570 need not be symmetric, nor have the same shape (skewness
 571 and kurtosis) as the magnitude of the output force increases.
 572 For some muscles the convergence accelerates after 60% or
 573 80% of task intensity (as in LUM and EIP), while others
 574 converge monotonically along the entire progression (e.g. DI
 575 and PI). The peaks (i.e. modes) of each histogram at each
 576 task intensity represents the slice of the polytope that has
 577 the largest relative volume along that muscle dimension (i.e.,
 578 greatest frequency of that level of muscle activation across all
 579 valid solutions). Importantly, for most muscles (FDP, FDS,
 580 EIP, EDC, and LUM), the mode is not necessarily located at
 581 the same relative level of activation needed for maximal force
 582 output. That is, the histogram at high levels of force is not
 583 simply a shifted version of the histogram at low levels of force.
 584 The histograms for DI are the exception, whose modes seem
 585 to scale linearly with task intensity.

586 These histograms, in conjunction with the results in the
 587 parallel coordinate visualization, also demonstrate that the
 588 structure of feasible activation spaces cannot be inferred from
 589 their bounding boxes alone (i.e., upper and lower activation
 590 bounds for each muscle). An immediate example is how,
 591 for most task intensities, both EIP and LUM have similar
 592 lower and upper bounds near 0 and 1, respectively—yet their
 593 distributions are thoroughly distinct.

594 **Author Affiliations.** Include department, institution, and complete address, with the ZIP/postal code, for each author. Use
 595 lower case letters to match authors with institutions, as shown
 596 in the example. Authors with an ORCID ID may supply this
 597 information at submission.

598 **Submitting Manuscripts.** All authors must submit their articles at [PNAScentral](#). If you are using Overleaf to write your
 599 article, you can use the “Submit to PNAS” option in the top
 600 bar of the editor window.

601 **Format.** Many authors find it useful to organize their manuscripts with the following order of sections; Title, Author
 602 Affiliation, Keywords, Abstract, Significance Statement, Re-
 603 sults, Discussion, Materials and methods, Acknowledgments,
 604 and References. Other orders and headings are permitted.

605 **Manuscript Length.** PNAS generally uses a two-column for-
 606 mat averaging 67 characters, including spaces, per line. The
 607 maximum length of a Direct Submission research article is six
 608 pages.

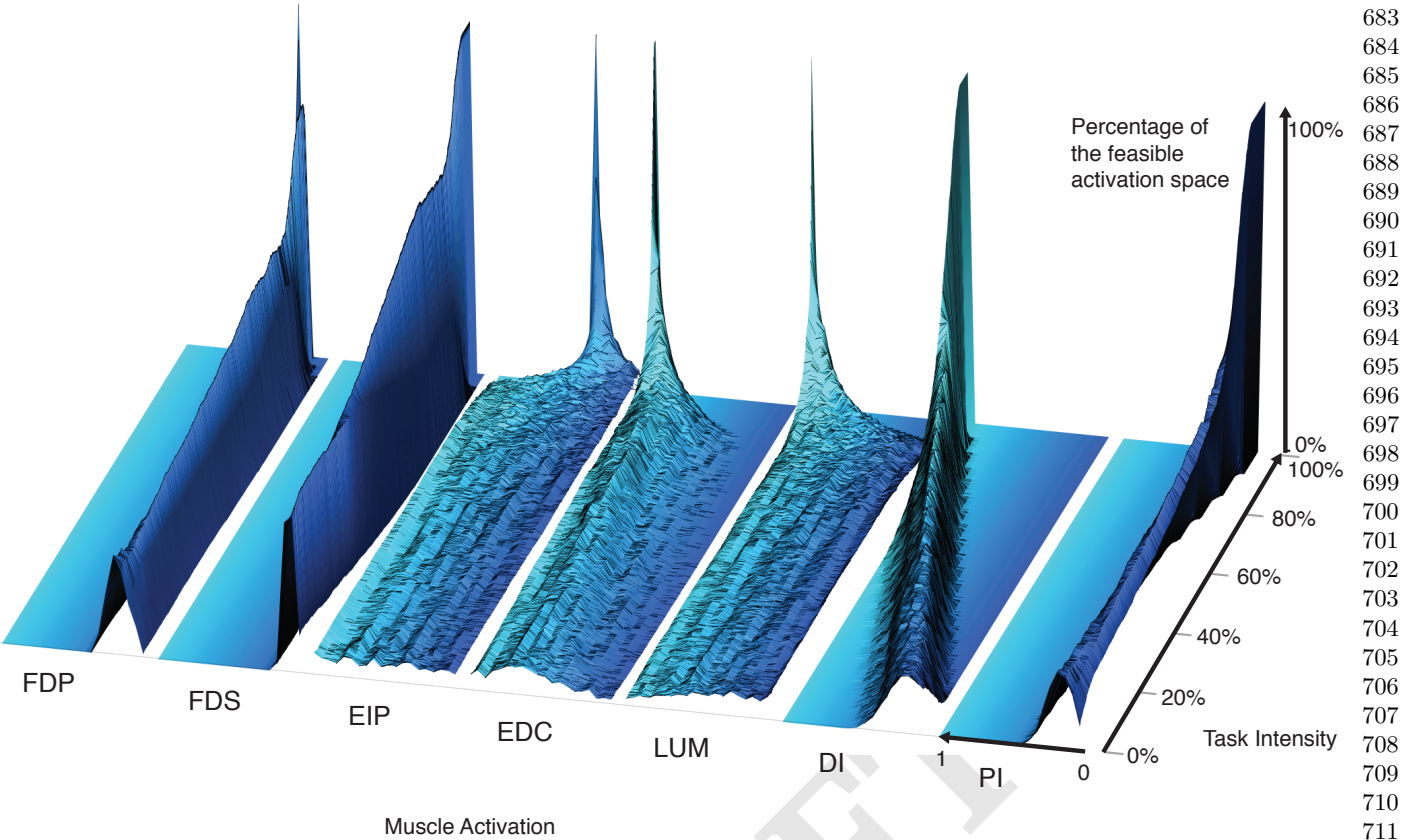


Fig. 7. The within-muscle probabilistic structure of feasible muscle patterns across 1,000 levels of fingertip task intensity. The changes in the breadth and height for each muscle reveal muscle-specific consequences of task intensity on their probability distributions. The cross-section of each density plot is the 50-bin histogram of activation for each muscle, at that task intensity. Height represents the percentage of solutions for that task. The axis going into the page indicates increasing fingertip task intensity up to 100% of maximal. Color is used to provide perspective.

pages and a PNAS PLUS research article is ten pages including all text, spaces, and the number of characters displaced by figures, tables, and equations. When submitting tables, figures, and/or equations in addition to text, keep the text for your manuscript under 39,000 characters (including spaces) for Direct Submissions and 72,000 characters (including spaces) for PNAS PLUS.

References. References should be cited in numerical order as they appear in text; this will be done automatically via bibtex, e.g. (?) and (? ?). All references, including for the SI, should be included in the main manuscript file. References appearing in both sections should not be duplicated. SI references included in tables should be included with the main reference section.

Data Archival. PNAS must be able to archive the data essential to a published article. Where such archiving is not possible, deposition of data in public databases, such as GenBank, ArrayExpress, Protein Data Bank, Unidata, and others outlined in the Information for Authors, is acceptable.

Language-Editing Services. Prior to submission, authors who believe their manuscripts would benefit from professional editing are encouraged to use a language-editing service (see list at www.pnas.org/site/authors/language-editing.xhtml). PNAS does not take responsibility for or endorse these services, and

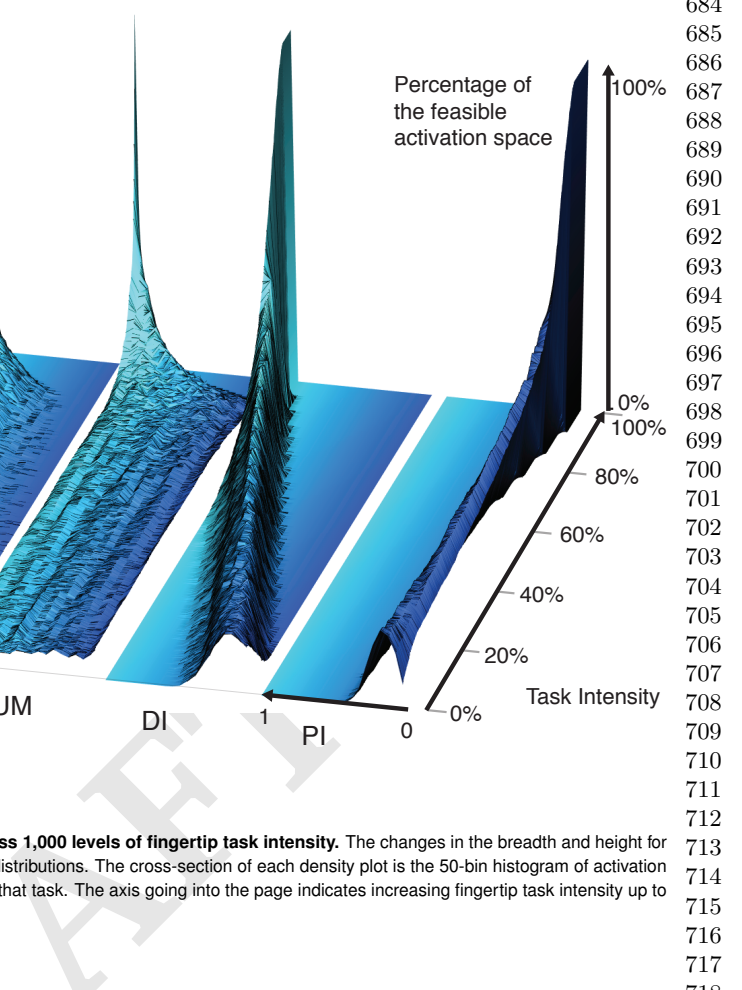


Fig. 8. Placeholder image of a frog with a long example caption to show justification setting.

their use has no bearing on acceptance of a manuscript for publication.

Digital Figures. Only TIFF, EPS, and high-resolution PDF for Mac or PC are allowed for figures that will appear in the main text, and images must be final size. Authors may submit U3D or PRC files for 3D images; these must be accompanied by 2D representations in TIFF, EPS, or high-resolution PDF format. Color images must be in RGB (red, green, blue) mode. Include the font files for any text.

Figures and Tables should be labelled and referenced in the standard way using the \label{} and \ref{} commands.

Figure 8 shows an example of how to insert a column-wide figure. To insert a figure wider than one column, please use the \begin{figure*}... \end{figure*} environment. Figures wider than one column should be sized to 11.4 cm or 17.8 cm wide.

Single column equations. Authors may use 1- or 2-column equations in their article, according to their preference.

To allow an equation to span both columns, options are to use the \begin{figure*}... \end{figure*} environment mentioned above for figures, or to use the